Journal of Energy Storage 152 (2026) 120719

Contents lists available at ScienceDirect

Journal of Energy Storage

journal homepage: www.elsevier.com/locate/est

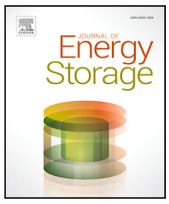

Research papers

Modeling of alkaline batteries and investigation of the relationship between electrochemical impedance and Raman spectroscopy

Marzio Barresi [a], Simone Barcellona [a,*], Cha Long [a], Lorenzo Codecasa [a], Marco Menegazzo [b], Rossella Yivlialin [b], Eugenio Gibertini [c], Andrea Lucotti [c], Gianlorenzo Bussetti [b], Samuele Grillo [a]

[a] Department of Electronics, Information and Bioengineering – Politecnico di Milano, Piazza Lonardo da Vinci, 32, Milano, 20133, Italy
[b] Department of Physics – Politecnico di Milano, Piazza Lonardo da Vinci, 32, Milano, 20133, Italy
[c] Department of Chemistry, Materials and Chemical Engineering – Politecnico di Milano, Piazza Lonardo da Vinci, 32, Milano, 20133, Italy

ARTICLE INFO

Keywords:
Alkaline batteries
Raman spectroscopy
Electrochemical impedance spectroscopy

ABSTRACT

This work presents an in-depth investigation of the electrochemical behavior of alkaline manganese dioxide batteries, focusing on the correlation between electrical and chemical characterizations through galvanostatic electrochemical impedance spectroscopy and Raman spectroscopy. A physics-based equivalent electric circuit model is proposed to capture the battery's impedance response at different state of charge (SOC) levels, accounting for ohmic resistance, charge-transfer processes, and diffusion phenomena. The evolution of the model parameters throughout the discharge process highlights critical transitions in internal battery dynamics, including the formation of zinc oxide layers and the increase in interfacial resistances. Concurrently, Raman spectroscopy measurements performed on the cathode surface at various SOC levels reveal significant structural and compositional changes, most notably the gradual transformation of manganese dioxide (MnO_2) into manganese(III) oxide (Mn_2O_3) and mixed zinc-manganese oxides with a spinel structure ($ZnMn_2O_4$) resulting from zinc migration through the separator. Finally, this work provides new insights into degradation mechanisms by establishing a direct correlation between electrical parameters and chemical transformations.

1. Introduction

The ever-growing demand for high-performance batteries has become a cornerstone of modern technology, driving advancements in portable electronics, electric vehicles, and renewable energy storage systems. As the transition toward cleaner energy sources accelerates, the role of batteries in enabling efficient energy storage and delivery becomes increasingly crucial [1]. However, despite ongoing progress in battery design, challenges related to performance degradation, capacity loss, and safety concerns persist and must be addressed to achieve reliable and long-lasting energy storage solutions [2].

Specifically, batteries can be classified into primary (non-recharge able) and secondary (rechargeable) types [3]. Primary batteries—such as alkaline, zinc–carbon, and lithium-based cells—are widely used in low-drain or intermittently operated devices like remote controls, clocks, electric toys, cameras, and smoke detectors. Their main advantages include long shelf life, low cost, and high energy density for short-term use. However, because they cannot be recharged, they generate higher environmental impact and require frequent replacement in long-term applications [4,5]. In contrast, secondary batteries—including lithium-ion, nickel–metal hydride, nickel–cadmium, and lead–acid chemistries—are commonly employed in applications that require frequent cycling or sustained power delivery [6,7].

Among primary batteries, alkaline batteries are particularly valued for their stability, safety, and cost-effectiveness [4]. Given their widespread use and importance, understanding the internal processes that influence their performance is crucial for optimizing efficiency, extending lifespan, and reducing environmental impact. A fundamental step toward improving battery performance is developing a comprehensive understanding of their behavior under real operating conditions. To this end, accurately modeling the different physical and electrochemical processes occurring within the battery is essential.

In the literature, numerous battery models have been proposed, particularly in recent decades for lithium-ion batteries. Broadly, these

* Corresponding author.
E-mail addresses: marzio.barresi@polimi.it (M. Barresi), simone.barcellona@polimi.it (S. Barcellona), lorenzo.codecasa@polimi.it (L. Codecasa), marco.menegazzo@polimi.it (M. Menegazzo), rossella.yivlialin@polimi.it (R. Yivlialin), eugenio.gibertini@polimi.it (E. Gibertini), andrea.lucotti@polimi.it (A. Lucotti), gianlorenzo.bussetti@polimi.it (G. Bussetti), samuele.grillo@polimi.it (S. Grillo).

https://doi.org/10.1016/j.est.2026.120719
Received 3 June 2025; Received in revised form 16 January 2026; Accepted 19 January 2026
Available online 22 January 2026
2352-152X/© 2026 The Authors. Published by Elsevier Ltd. This is an open access article under the CC BY-NC-ND license (http://creativecommons.org/licenses/by-nc-nd/4.0/).

models can be classified into two main categories: physical models and equivalent electric circuit (EEC) models [8]. Physical models provide high accuracy but require substantial computational resources, as they involve solving multiple partial differential equations. Conversely, EEC models are less accurate but considerably simpler, since they rely on algebraic and ordinary differential equations [9].

Focusing on alkaline batteries, within the category of physical models, Wruck et al. [10] developed a one-dimensional macrohomogeneous model describing the galvanostatic discharge of a planar alkaline electrolytic manganese dioxide (MnO_2) cathode immersed in a 9 M potassium hydroxide (KOH) solution. The model accounted for electrolyte concentration gradients using dilute-solution theory, while migration and convection effects were neglected, and the potential distribution was assumed to follow Ohm's law—an assumption that conflicts with the concentration-dependent conductivity reported in [11]. Later, the authors in [12,13] applied a similar macrohomogeneous framework to model the discharge of a cylindrical primary alkaline battery, incorporating the anode, separator, and cathode. Their cathode model treated electrolytic MnO_2 as nonporous spherical particles surrounded by concentrated KOH, resembling a "grain model". This pseudo-two-scale approach coupled surface-reaction kinetics with mass transport within the cathode pores, though its accuracy was limited, particularly during the early and mid-stages of discharge. Subsequent refinements in [14,15] introduced the influence of zincate species in the electrolyte and enabled simulation of different discharge modes. Further advancements by the authors in [16,17] incorporated semi-analytical expressions for the open-circuit voltage (OCV) and a discharge coefficient, resulting in improved agreement with experimental data under various operating conditions. Farrell et al. [18] proposed a one-dimensional model for the porous annular cathode that extended earlier approaches [12,14] by accounting for the bidisperse nature of the electrode's pore structure. They described the cathode as aggregates of porous electrolytic MnO_2 particles, containing both micropores within the particles and macropores between them, through which mass transport occurs. The model incorporated three coupled scales—macroscopic, microscopic, and submicroscopic—and treated the solid matrix as two distinct phases, graphite and MnO_2, each with its own physical properties. This framework provided a more detailed representation of the discharge behavior of alkaline electrolytic MnO_2 cathodes.

Regarding EEC models, only a limited number of studies in the literature have focused on alkaline batteries. In [19], the authors proposed an EEC model in which the various components of the battery—such as the current collectors, bulk MnO_2, electrolyte, and the MnO_2/electrolyte interface—along with the associated faradaic and non-faradaic processes of the MnO_2 cathode, are represented using classical resistors (R), capacitors (C), and constant phase elements (CPEs). Similarly, in [20], the authors developed three distinct EEC models for the MnO_2 cathode, each corresponding to a different frequency range, to capture variations in both the manganese dioxide properties and the electrode porosity. In [21], the authors used the well-known Randles circuit to model the MnO_2 cathode, in which titanium dioxide was added. In [22], a comprehensive EEC model of an alkaline battery was introduced, in which both the anode and cathode are represented by the same RC and CPE elements but arranged in different configurations—resembling one of the equivalent circuit models commonly used for lithium-ion batteries. On the other hand, for other types of primary batteries, such as zinc–carbon cells, the EEC models employed are similar [23,24].

To analyze battery behavior and characterize both physical and EEC models, tests can be conducted from both electrical and chemical perspectives.

From an electrical standpoint, battery tests are generally categorized into time-domain and frequency-domain approaches. Among the time-domain methods, the galvanostatic intermittent titration technique (GITT) and hybrid pulse power characterization (HPPC) tests are the most commonly employed. In GITT, the battery is subjected to partial discharges followed by rest periods to allow electrochemical relaxation, enabling the determination of the OCV curve or the estimation of internal resistance. The HPPC test is similar, but involves a sequence of high-power charge and discharge pulses to evaluate the dynamic performance of the battery. Within frequency-domain approaches, electrochemcal impedance spectroscopy (EIS) has emerged as a powerful diagnostic tool, providing the frequency response of an electrochemical device and offering insights into charge-transfer processes, electrode kinetics, and degradation mechanisms [25–27]. Specifically, EIS can be performed as galvanostatic EIS (GEIS), where a small sinusoidal current is applied, or as potentiostatic EIS, where a small sinusoidal voltage is imposed. In both cases, the resulting voltage or current response is measured to derive the electrical impedance. Because the battery is a non-linear system, the amplitude of the applied current or voltage must be small enough to maintain near-equilibrium conditions, yet sufficiently large to avoid a low signal-to-noise ratio [28]. Only a few studies in the literature have applied EIS to alkaline batteries [19,20,22,29]. In [19], the authors performed EIS measurements under various conditions, such as external pressure, electrolyte content, and the presence of additives. Based on these results, they modeled the MnO_2 cathode of the alkaline battery using an EEC model and providing their own physical interpretations. Their analysis showed that the battery impedance decreased with reduced electrode thickness and increased pressure and electrolyte content. In [20], EIS was employed to investigate the electrochemical behavior and morphological evolution of alkaline manganese dioxide cathodes during discharge. The analysis revealed an intermediate-frequency inductive loop (2–50 Hz) not previously reported in the literature. This feature, along with the high- and low-frequency EIS responses, was interpreted as evidence of changes in the MnO_2 structure, electrode porosity, and mechanical degradation of the active material. The study showed that as the manganese dioxide becomes increasingly reduced, structural expansion induces particle cracking and porosity changes within both the particles and the electrode, making part of the material inactive for H^+ ions insertion. In [22], the authors conducted multiple EIS tests on different brands of alkaline batteries, discharging them under various profiles to compare their performance and cost, using a model similar to those employed for lithium-ion batteries. Nevertheless, they did not provide a complete description or trend of the parameters as a function of the battery discharge. In [29], the authors proposed a combined mechanical–electrochemical testing procedure, performing EIS measurements under various external loading conditions to investigate the electrochemical behavior of alkaline batteries subjected to mechanical stress. This integrated approach enabled detailed monitoring of electrochemical changes caused by mechanical deformation and allowed differentiation between various battery cell geometries. Comparative analysis of force–displacement and voltage–displacement showed geometry-dependent failure modes and highlighted the influence of loading rate.

However, a comprehensive understanding of battery behavior requires more than electrical analysis alone. The chemical and structural evolution of electrode and electrolyte materials during operation plays a critical role in determining overall performance. Integrating electrochemical measurements with insights into structural and compositional changes enables a more holistic assessment of degradation phenomena and functional limitations. In particular, tracking how chemical and structural transformations occur during discharge is essential, as these processes directly affect efficiency, capacity, lifespan, and safety. Degradation mechanisms—such as electrode dissolution, electrolyte decomposition, and the formation of unwanted byproducts—can progressively reduce battery effectiveness, ultimately limiting practical applications. Capturing these dynamic processes at the local scale, in real time, and with chemical specificity remains a significant challenge in battery research [30]. Advanced analytical techniques are therefore required to probe internal battery components with high spatial and chemical resolution. In practice, this often involves disassembling the

cell and extracting sections of the cathode or anode. Such procedures inevitably destroy the sample and produce specimens that are non-uniform in size and morphology, frequently exhibiting significant surface roughness. Nonetheless, detailed chemical characterization of these heterogeneous materials is essential for elucidating reaction pathways and degradation mechanisms. These challenges render many conventional surface science techniques unsuitable for such analyses.

From a chemical perspective, Raman spectroscopy (RS) represents a particularly powerful tool in this context, offering a non-destructive means to probe local chemical compositions, phase transitions, and reaction dynamics within electrodes and electrolytes [31]. RS is based on the interaction between light and the molecular bonds within a material. It operates as a light-scattering technique in which molecules scatter photons from an intense laser source. The majority of the scattered light retains the same wavelength as the incident beam—known as Rayleigh scattering—and carries no chemical information. However, a very small fraction of the scattered photons undergo a wavelength shift that depends on the molecular structure of the sample; this phenomenon is referred to as Raman scattering. A Raman spectrum displays a series of peaks that represent the intensity and wavelength of the Raman-scattered light. Each peak is associated with a particular vibrational mode of molecular bonds as well as collective vibrations involving groups of atoms, including polymer chain vibrations, and lattice oscillations. RS has demonstrated exceptional versatility, particularly in its ability to be integrated with other experimental methods—such as scanning probe microscopy and electrochemical measurements—to provide a more comprehensive understanding. Moreover, with precise positioning and focusing of the laser spot, RS can be effectively applied to small, irregular, and rough samples, enabling the in-depth characterization of complex composite materials. In doing so, it facilitates deeper insight into the physicochemical changes occurring during battery discharge, shedding light on key factors that govern performance, degradation, and failure mechanisms. Focusing on alkaline batteries, only a few studies in the literature have conducted RS on them. Specifically, in [32], the authors investigated the structural evolution of the zinc oxide (ZnO) passive layer formed on zinc (Zn) electrodes in a cylindrical alkaline battery using RS. The authors modified the battery cell by replacing one end with an optical window while maintaining all other commercial components. Experimental results were recorded at different discharge levels by discharging the battery at a high current rate, revealing the formation of crystalline ZnO, in particular at the end of the discharge, with no detectable zinc hydroxide phase observed throughout the process. In [33], the Raman spectra of nanostructured manganese(II,III) oxide (Mn_3O_4) were analyzed, and the correlations between Raman shift, bandwidth, and particle size were determined. The results indicate that the observed spectral shifts and peak broadening primarily arise from grain size effects. Overall, RS proves to be a simple and effective technique for estimating the size of certain nanomaterials. In [34], RS was applied to investigate the structural and vibrational properties of manganese oxide. This technique allowed for detailed characterization of manganese oxide phases that are often difficult to distinguish using conventional methods such as X-ray diffraction. The analysis aimed to identify the characteristic Raman features of manganese oxide and provided reference data useful for understanding its behavior in various electrochemical and material science applications. In [35], the authors performed RS on various structures of manganese oxide mineral species, showing that, by using different laser wavelengths in combination with a database of standard spectra, it was possible to identify different phyllomanganate minerals. Specifically, the wavelength range of approximately 630–665 cm^{-1} was found to be strongly correlated with the presence of Mn^{3+} ions.

Nevertheless, mechanistic studies and comprehensive reviews indicate that capacity fade and increases in internal resistance primarily result from the formation of electrochemically inert Zn-bearing phases, as mixed zinc-manganese oxides with a spinel structure $ZnMn_2O_4$, manganese oxide compounds, and secondary reaction products that impede ionic transport or induce electrical isolation of active material [36]. Consequently, strategies aimed at limiting uncontrolled Zn deposition or accumulation at the cathode—through electrolyte engineering, pH optimization, additive use, or pre-intercalation techniques—are commonly employed to suppress $ZnMn_2O_4$ formation. This suppression improves cycle life by reducing internal resistance and restoring reversible Zn^{2+} ions transport characteristics [37].

Crucially, our study provides the first direct experimental connection between these macroscopic phenomena (current–voltage behavior) and the specific microscopic degradation mechanisms at the cathode. Electrical characterization of various battery cell samples reveals the macro-level effects of degradation, specifically the observed increases in internal resistance and capacity fade. Concurrently, RS analysis of cathode material from the same samples offers molecular-level evidence, confirming the gradual reduction of MnO_2 into Mn_2O_3 and progressive formation of $ZnMn_2O_4$ as a function of cycling and degradation state. By correlating quantitative changes in Raman signal intensity—indicative of $ZnMn_2O_4$ abundance—with electrical metrics such as charge-transfer resistance and capacity loss, we establish, for the first time, a clear and direct link between Zn-compound formation and the measurable deterioration of the cell's current–voltage characteristics. This correlation firmly positions Mn_2O_3 and $ZnMn_2O_4$ formation as primary, quantifiable drivers of performance decay in these batteries.

In light of the above, the primary objective of this work is to find a bridge between the results obtained from two well-known techniques—RS and GEIS—to enhance electrical modeling for simulations and provide manufacturers with criteria to identify potential physicochemical improvements. Specifically, Raman analysis was performed on the MnO_2 cathode at different SOC levels alongside GEIS measurements, enabling a direct correlation between macroscopic electrical signals and local, microscopic chemical changes occurring in the cathode material. These changes, on one hand, help elucidate the mechanisms at the solid–liquid interface and the formation of surface barriers that can impede charge transfer; on the other hand, this experimental approach offers insights into material evolution during the discharge process, providing valuable information for developing strategies to prevent or mitigate battery aging. Such knowledge has significant implications for the environment, industrial battery manufacturing protocols, and overall economic efficiency.

To this end, nine cylindrical alkaline battery cells were tested. They underwent partial discharge and GEIS measurements, and were disassembled at different SOC levels to perform RS. The results were analyzed from both electrical and chemical perspectives, establishing a link between the macroscopic observations from GEIS and the microscopic insights obtained from RS. As in most of the previously mentioned studies in the literature, all tests and analyses in the present work were conducted at room temperature.

Finally, an EEC model typically used for lithium-ion batteries was adapted for alkaline batteries, offering a possible physical interpretation of its parameters, while the actual variation of these parameters as a function of SOC was derived.

2. Battery model

Alkaline batteries generate power through electrochemical reactions taking place at their electrodes. The key materials facilitating these reactions include Zn as the anode (negative electrode), MnO_2 as the cathode (positive electrode), and KOH as the electrolyte [38]. Several authors [39,40] describe the overall discharge reactions of alkaline batteries as relatively complex, involving multiple intermediate products. However, the fundamental discharge processes at the anode and cathode can be summarized more simply.

At the anode, Zn undergoes oxidation, meaning it donates electrons. This oxidation process can be represented as a two-step reaction:

$$\begin{aligned} &Zn(s) + 4OH^-(aq) \rightarrow Zn(OH)_4^{2-}(aq) + 2e^- \\ &Zn(OH)_4^{2-}(aq) \rightarrow ZnO(s) + 2OH^-(aq) + H_2O(l). \end{aligned} \quad (1)$$

At the cathode, MnO_2 undergoes reduction, meaning it gains electrons. Simultaneously, water (H_2O) molecules decompose at the oxide/electrolyte interface within the particle, leading to the intercalation of H^+ ions into the oxide lattice. The cathodic reaction of MnO_2 proceeds through a two-step process:

$$\begin{aligned} &2MnO_2(s) + 2H_2O(l) + 2e^- \rightarrow 2MnO(OH)(s) + 2OH^-(aq) \\ &2MnO(OH)(s) \rightarrow Mn_2O_3(s) + H_2O(l). \end{aligned} \tag{2}$$

By combining the half-reactions occurring at the anode and cathode, the overall reaction governing the operation of an alkaline battery can be obtained:

$$Zn(s) + 2MnO_2(s) \rightarrow ZnO(s) + Mn_2O_3(s). \tag{3}$$

In the overall reaction, Zn at the anode reacts with MnO_2 at the cathode and H_2O from the electrolyte, leading to the formation of ZnO and Mn_2O_3. The transfer of electrons from Zn to MnO_2 through the external circuit generates electrical energy. KOH plays a crucial role in these reactions by supplying the OH^- ions required at both the anode and cathode. The movement of these ions within the electrolyte maintains charge balance and enables the continuous flow of electrons through the external circuit, allowing the battery to power connected devices.

As discussed in the introduction, numerous research studies on battery modeling can be found in the literature, with a particular focus on lithium-ion batteries [41]. Although the present study focuses on alkaline batteries, it is worth briefly reviewing relevant literature on lithium-ion batteries, which have been extensively investigated in recent years and share several underlying electrochemical principles that can inform the present analysis. Specifically, numerous EEC models have been proposed for lithium-ion batteries, ranging from simple to highly complex configurations [41]. The level of complexity depends on the desired accuracy, ranging from basic structures to sophisticated models that account for multiple time constants and nonlinear effects. The simplest model consists of an ideal voltage source—representing the OCV and corresponding to the voltage at thermodynamic equilibrium—in series with a resistor accounting for the total internal resistance [42,43]. While easy to implement, this two-parameter model cannot adequately capture the battery's dynamic behavior and is therefore unsuitable for applications requiring higher accuracy. To overcome this limitation, the widely used Thevenin model was introduced [44,45]. This model extends the basic EEC representation by including one or more parallel RC branches in series with the high-frequency internal resistance, thereby enabling the dynamic response of the battery to be modeled. Increasing the number of RC branches enhances model accuracy, and the simplest EEC model can be regarded as a special case of the Thevenin model with zero RC branches [46]. More advanced EEC models have been developed, for example in [47,48]. Specifically, in [48] one of the most comprehensive models is presented. This model, like the previous ones, includes an ideal voltage source representing the OCV of the battery. In practice, this voltage depends on the SOC; therefore, its behavior is associated with a large chemical capacitance. It also incorporates a high-frequency internal resistance that accounts for the ohmic resistance of the electrodes, electrolyte, separator, and current collectors. Additionally, the model includes a ZARC element (a CPE connected in parallel with a resistor) that represents the solid electrolyte interphase (SEI) layer formed on the anode surface as a result of electrolyte reduction. This element corresponds to the first semicircle in the Nyquist plot, appearing at medium-to-high frequencies. A second ZARC element accounts for the charge-transfer resistance and the double-layer capacitance at the electrode/electrolyte interface, appearing as the second semicircle in the Nyquist plot at medium-to-low frequencies. Finally, a finite-length Warburg impedance is incorporated to describe ion diffusion within the active materials of the electrodes and the electrolyte. According to the literature, three main types of Warburg elements are commonly employed to represent lithium or lithium-ion diffusion phenomena.

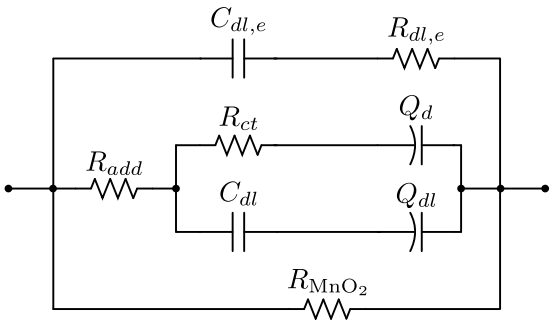

Fig. 1. Battery model proposed in [19].

The first is the semi-infinite Warburg element, which characterizes diffusion through a semi-infinite medium and appears in the Nyquist plot as a straight line inclined at 45°. The second type is the finite-space Warburg element, which models diffusion within a confined layer bounded by an impermeable interface. In the Nyquist plot, it initially appears as a 45° diagonal line that transitions into a vertical segment representing the capacitive response of the system. The third type, the finite-length Warburg element, describes diffusion within a bounded layer whose far boundary is permeable or transmissive. In the Nyquist plot, it begins as a 45° line and then transitions into a large semicircular arc. From a physical standpoint, since the electrodes represent a reflexive boundary, the finite-space Warburg element should be the most suitable choice to model this behavior. Nevertheless, many models (as in [48]) use the finite-length Warburg element, which exhibits a similar trend in the initial part of the low-frequency region. However, the latter portion, represented by a semicircle in the Nyquist plot, overlaps with the OCV modeled by an ideal voltage source controlled in charge that describes the battery capacitive behavior at very low frequencies.

In contrast, the literature on battery models for alkaline batteries is relatively limited. In [19], the authors analyzed an alkaline battery and proposed an EEC model for the cathode, assigning physical meaning to each circuit element. This model is shown in Fig. 1. Fundamentally, charge transport within the electrode occurs through three parallel pathways. The first is the electronic pathway through the manganese dioxide particles, represented by the resistance $R_{\mathrm{MnO_2}}$. The second pathway is ionic, occurring through the electrolyte, and is characterized by the resistance $R_{dl,e}$ and the corresponding double-layer capacitance $C_{dl,e}$. The third pathway involves charge transfer at the manganese dioxide/electrolyte interface. This contribution consists of the charge-transfer resistance R_{ct} in series with a CPE whose pseudo-capacitance Q_d models diffusion through the porous structure of manganese dioxide, and in parallel with the double-layer capacitance C_{dl} in series with another CPE whose pseudo-capacitance Q_{dl} captures the double-layer effect. Additionally, a resistance R_{add} is included in series to account for charge-transport processes occurring in either the solid phase or the electrolyte before and after the charge-transfer event.

On the other hand, in [22], the authors employed an EEC model similar to that reported in [48] for lithium-ion batteries, with the main difference being the use of a semi-infinite Warburg element instead of a finite-length one. Although the authors did not explicitly discuss their rationale, the use of a lithium-ion battery model for alkaline batteries can be justified by the analogous operating principles of the two chemistries. Following this reasoning, in the present study, the lithium-ion battery model from [48] was adapted for application to alkaline batteries, based on the similarity of their fundamental electrochemical mechanisms and providing a possible physical interpretation of its components. However, for the sake of simplicity, the finite-length Warburg impedance was replaced with a simple RC parallel branch. Although this choice may reduce the model accuracy at very low frequencies, it offers the advantage of a simpler structure that still

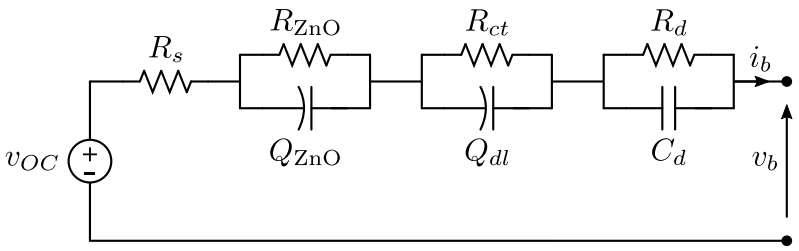

Fig. 2. Proposed battery model.

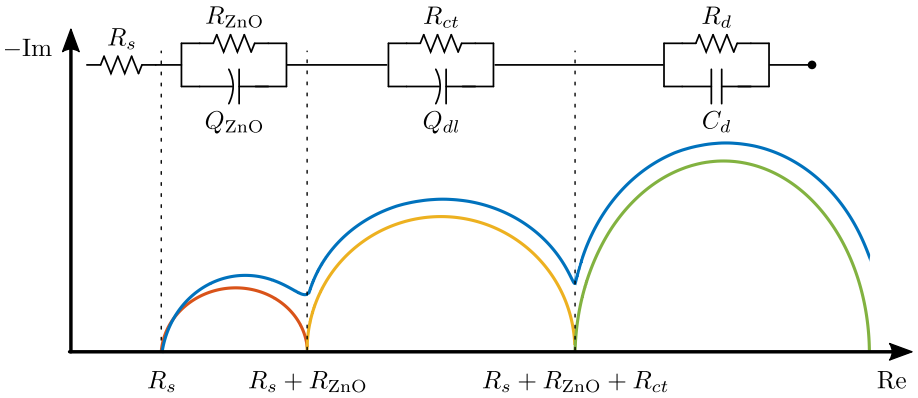

Fig. 3. Nyquist plot of proposed model.

captures the general trend of the parameters related to the diffusion process [49].

The proposed model is reported in Fig. 2. Specifically, v_{OC} denotes the OCV of the battery, while R_s represents the high-frequency ohmic resistance of the battery components, as in lithium-ion batteries. In contrast to lithium-ion batteries, which feature a SEI layer, alkaline batteries develop a ZnO layer that, although different in composition and function, can be considered the analogous component. This layer is modeled using the resistance R_{ZnO} and the pseudo-capacitance Q_{ZnO}, along with its associated depression factor β_{ZnO}. The charge-transfer resistance and double-layer capacitance associated with both electrodes are represented by the resistance R_{ct} and the pseudo-capacitance Q_{dl}, respectively, along with their corresponding depression factor $\beta_{ct/dl}$. These components, on one hand, model the intercalation of hydrogen ions (H^+) into the oxide lattice—analogous to lithium-ion intercalation/deintercalation in lithium-ion batteries—and, on the other hand, the oxidation reaction of Zn at the anode. Finally, the diffusion of OH^- ions in the electrolyte and H^+ ions in the cathode is represented by the diffusion resistance R_d and diffusion capacitance C_d. The total battery impedance, Z_{tot}, is then expresses as follows:

$$Z_{tot} = R_s + \frac{R_{\mathrm{ZnO}}}{1 + (j \cdot \omega)^{\beta_{\mathrm{ZnO}}} \cdot R_{\mathrm{ZnO}} \cdot Q_{\mathrm{ZnO}}} + \\ + \frac{R_{ct}}{1 + (j \cdot \omega)^{\beta_{ct,dl}} \cdot R_{ct} \cdot Q_{dl}} + \frac{R_d}{1 + j \cdot \omega \cdot R_d \cdot C_d} \tag{4}$$

where ω is the angular frequency in rad/s.

In the frequency domain, these elements correspond to different regions of the Nyquist plot, visible in Fig. 3. Specifically, the resistance R_s corresponds to the intersection with the real axis. The first small semicircle in the high-medium frequency range can be interpreted as the complex impedance related to the properties of ZnO. Meanwhile, the larger semicircle in the medium frequency range can represent the charge-transfer and double-layer effects at the two electrode/electrolyte interfaces. Finally, the low-frequency region of the Nyquist plot can be associated with the diffusion processes of OH^- ions in the electrolyte and H^+ ions in the cathode.

Table 1
Battery specifications.

Parameter	Value
Nominal capacity (2 mA, 5 V cut-off)	726 mAh
Typical Voltage	9 V (at 20 °C)
AC impedance @ 1kHz	1.692 Ω

3. Test procedure and experimental setup

The present study examined the Procell PX1604, a commercially available alkaline manganese dioxide battery, as detailed in Table 1. This battery operates at a standard voltage of 9 V under normal conditions of 20 °C and has a rated capacity of 726 mAh when discharged at a 2 mA rate. It reaches the end of its operational life when its voltage drops to the cut-off value of 5 V. Specifically, this study aims to characterize the battery at different SOC levels, ranging from the fully charged to the fully discharged state, under a constant room temperature of 20 °C.

Typically, this type of battery comes in either a stacked or cylindrical cell configuration. The Procell PX1604 battery pack specifically consists of six individual cylindrical cells connected in series, with each cell supplying 1.5 V and having a nominal capacity of 726 mAh at a 2 mA discharge rate.

Specifically, nine cylindrical cells were utilized, discharged, and analyzed at different SOC levels. Subsequently, these cells were disassembled for further examination. Two types of tests were conducted: GEIS measurements for electrical characterization and RS for chemical characterization. Table 2 reports the cells used in this analysis, their numbering, and the corresponding tests performed.

The GEIS experiments were conducted using an SP-150e potentiostat (Biologic Science Instruments) controlled via EC-Lab software installed on a PC connected to the instrument through an Ethernet cable.

For RS acquisition, the setup included three remotely selectable laser sources (473 nm, 532 nm, and 633 nm) and a spectrometer (NT-MDT NTEGRA Spectra) coupled with an Andor detector cooled to

−60 °C via a Peltier junction. Two optical objectives (20× and 40×) were available, with the 40× objective preferred for these experiments due to its higher numerical aperture (0.75). The red laser source (633 nm) was employed for all Raman measurements.

Cell characterization involved performing GEIS and RS tests as follows[1]: for each of Cells 1–9, a target SOC was predefined to determine when the cell would be opened for RS analysis, as reported in Table 2. The predefined opening SOC levels for the nine cells were 100%, 70%, 60%, 50%, 40%, 30%, and 0%.

Specifically, GEIS measurements were performed at the predefined opening SOC levels for Cells 1–6. For the fully discharged Cells 7–9, GEIS measurements were conducted across SOC levels from 100% to 0%, with data collected at 10% of SOC intervals. Even though certain cells were subjected to GEIS measurements only at specific SOC values corresponding to the openings for RS, by combining data from different cells tested at different SOC levels, the overall dataset provides coverage across a range of SOC values and captures the inherent cell-to-cell variability. The different SOC levels were achieved by discharging the cells at a low current of 2 mA. The cells were then allowed to rest for one hour to reach steady state, accounting for diffusion phenomena. Subsequently, GEIS measurements were conducted with a sinusoidal current of 2 mA (0.002C) over a frequency range from 100 mHz to 10 kHz, with two measurements averaged at each frequency point. In particular, the amplitude of the applied sinusoidal current was selected to ensure a sufficiently high signal-to-noise ratio in the voltage measurements, while maintaining the battery operation within its linear region. Moreover, the upper frequency threshold was chosen to reach the region of the frequency response where the behavior begins to exhibit inductive characteristics due to the cable connections. Conversely, the lower frequency threshold was set to a typical value that allows analysis of the medium-to-high frequency behavior while maintaining stable measurements. On the other hand, at very low frequencies, measurements take longer, which can disturb the battery steady state and potentially lead to measurement instability [50–52]. Nevertheless, the selected frequency range is commonly employed in other battery studies [53,54].

For the RS measurements, cells were initially examined with the 20× objective to identify relatively flat regions suitable for analysis. The 40× objective was then used for RS acquisition. Each spectrum was acquired with an average integration time of a few minutes, and the laser power impinging on the sample was kept below 0.6 mW to prevent any damage. To evaluate the reproducibility of RS, the following experimental protocol was adopted: (i) Cells 7, 8, and 9 at the same SOC were analyzed to assess the overall Raman response and to confirm the presence of characteristic vibrational features (e.g., $ZnMn_2O_4$ and/or the graphitic G and D bands); (ii) for each cell at different SOC levels, RS spectra were collected from multiple regions (approximately five) of the extracted cathode material. Due to the intrinsic surface roughness and slight compositional inhomogeneities observed under optical microscopy, variations in absolute peak intensities were detected. Nevertheless, all principal spectral features characteristic of each specific discharge state were consistently observed across the analyzed regions. Among the different internal components of the cell, the cathode was selected for investigation, as it exhibited relatively uniform regions after extraction. In contrast, the anode was unstable in air, becoming bluish and dusty within minutes, and the separator was largely torn upon opening the battery, precluding systematic analysis. The Raman spectral regions were chosen according to [55], which provides detailed identification of Zn- and Mn-containing compounds that evolve with cell discharge. The optical objective was selected to achieve an optimal balance between maintaining adequate laser focus on the highly roughened surface and enabling clear differentiation among the various regions of the extracted cathode material. The overall experimental procedure for the cells under test is summarized in the flowcharts shown in Fig. 4, while the experimental setups adopted for GEIS measurements and RS are shown in Fig. 5.

[1] The raw experimental impedance spectroscopy and rest-voltage interval datasets used in this work are publicly available in a dedicated GitHub repository: https://github.com/marzio-barresi/Electrical-Datasets-Alkaline-Batteries.git

Table 2
Battery Test matrix.

Cell	SOC	Tests
1	100%	GEIS and RS
2	70%	GEIS and RS
3	60%	GEIS and RS
4	50%	GEIS and RS
5	40%	GEIS and RS
6	30%	GEIS and RS
7	0%	GEIS (each 10% of SOC) and RS
8	0%	GEIS (each 10% of SOC) and RS
9	0%	GEIS (each 10% of SOC) and RS

4. Experimental results

4.1. Electrical parameters and results analysis

According to the test procedure described in the previous section, the cells were discharged at a constant current until reaching a predefined SOC level, followed by a one-hour rest period before conducting the GEIS measurements. For example, Fig. 6 shows the complete discharge voltage profile of Cell 7, where the discharge and rest periods are clearly distinguishable.

Fig. 7 shows the Nyquist plot of the GEIS measurements for Cell 7 at various SOC levels, while Figs. 8 and 9 separately present the Nyquist plots for Cells 1–9 at each SOC level. As observed, the impedance of the fresh cells is notably higher compared to other SOC levels, likely due to passivation of the Zn powder during storage or adsorption of organic corrosion inhibitors on the Zn surface. Comparing the spectra at 100% (Fig. 8(a)) and 90% (Fig. 8(b)) of SOC, a significant difference in impedance is evident, likely caused by the instability of the electrochemical state. Specifically, at 100% of SOC, the large semicircle may be attributed to higher-than-normal internal electrode resistance and cell-interface capacitance, as reported in [22]. Therefore, at high SOC levels, and in particular at 100% of SOC, even small cell-to-cell differences can result in significant variations in the GEIS response. Indeed, from Figs. 7 and 8, it can be observed that at high SOC levels, the GEIS spectra of different cells differ noticeably, whereas at low SOC levels, the spectra become very similar.

Based on the obtained GEIS measurements, two distinct semicircles are observed in the frequency range from 100 mHz to 10 kHz. According to the literature [29], no SEI layer forms in alkaline manganese dioxide batteries. Nevertheless, as the SOC decreases, ZnO growth occurs at the anode–electrolyte interface. Therefore, as hypothesized in Section 2, the smaller semicircle at higher frequencies can be attributed to the complex impedance associated with the ZnO layer at the anode, while the larger semicircle at lower frequencies likely corresponds to the charge-transfer and double-layer effects at both electrode–electrolyte interfaces.

Therefore, within the selected frequency range, the parameters corresponding to the high-frequency resistance and the two ZARC elements in model (4) were identified from the GEIS measurements (frequency-domain characterization), whereas the RC parameters associated with diffusion phenomena—which are not apparent in the GEIS results—were determined in the time domain from the transients observed during the relaxation periods (time-domain characterization), as shown in Fig. 10.

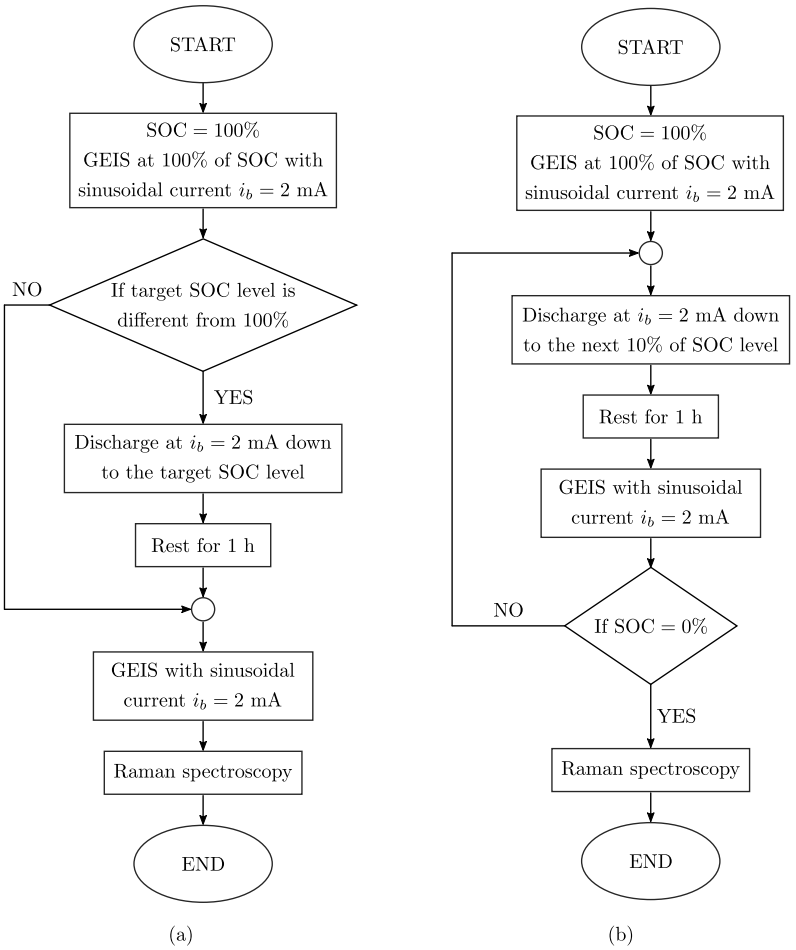

Fig. 4. Flowchart of the experimental procedure: (a) Cells 1–6; (b) Cells 7–9.

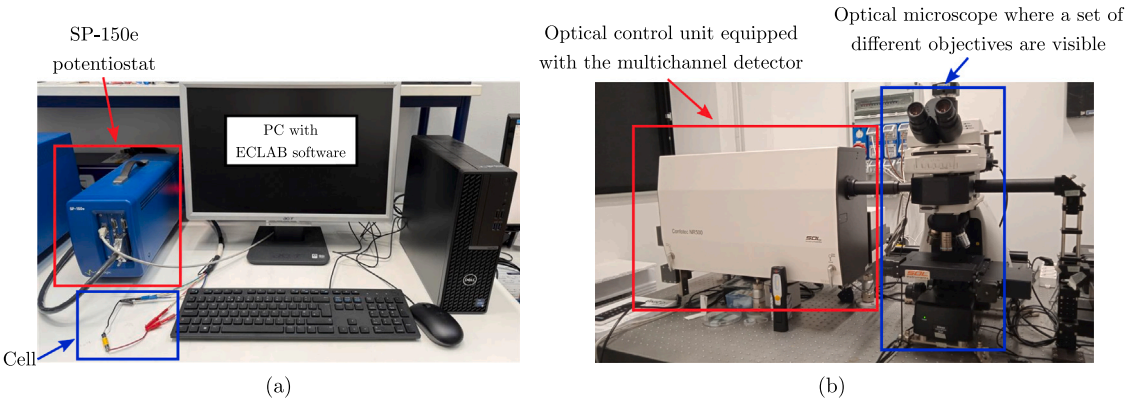

Fig. 5. Experimental setups used in this work: (a) configuration for GEIS measurements; (b) configuration for RS measurements.

4.1.1. Frequency-domain characterization

The parameters R_s, R_{ZnO}, Q_{ZnO}, β_{ZnO}, R_{ct}, Q_{ct}, and $\beta_{ct,dl}$ were determined by fitting the experimental GEIS data to model (4) using a complex least-squares minimization approach, while excluding the parallel RC branch associated with diffusion phenomena. To minimize the error of a complex quantity, the *fminsearch* function in MATLAB was employed with the following total vector error:

$$\epsilon = \sqrt{\left(\frac{\|\boldsymbol{R}_p - \boldsymbol{R}_p^*\|}{\|\boldsymbol{R}_p^*\|}\right)^2 + \left(\frac{\|\boldsymbol{X}_p - \boldsymbol{X}_p^*\|}{\|\boldsymbol{X}_p^*\|}\right)^2} \tag{5}$$

where $\boldsymbol{R}_p^*$ and $\boldsymbol{X}_p^*$ are the vectors containing the experimental data, while $\boldsymbol{R}_p$ and $\boldsymbol{X}_p$ are the vectors containing the modeled data.

4.1.2. Time-domain characterization

The parameters related to diffusion phenomena, R_d and C_d, were determined in the time domain by fitting the electrical transients observed during the relaxation periods corresponding to the SOC interval of 90%–0%. Obliviously, the values at 100% of SOC are missing because the first rest phase occurred when the battery reached 90% of SOC. This fitting was performed using the *fit* function in MATLAB, which applies a nonlinear least-squares optimization based on the

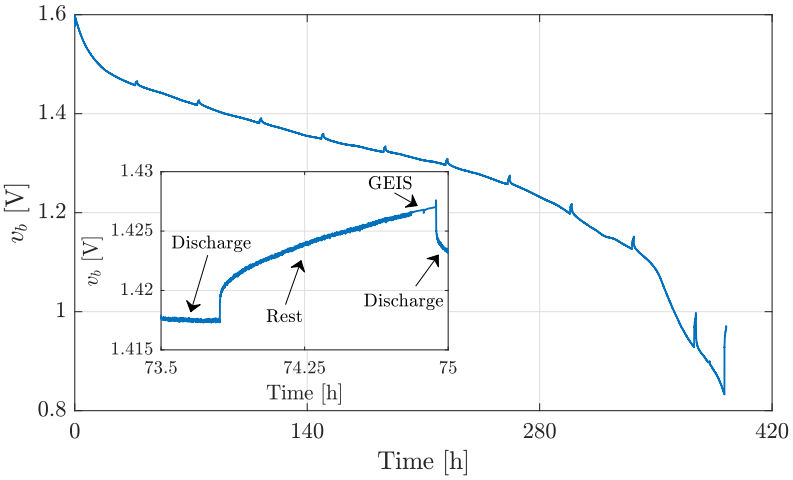

Fig. 6. Battery voltage profile.

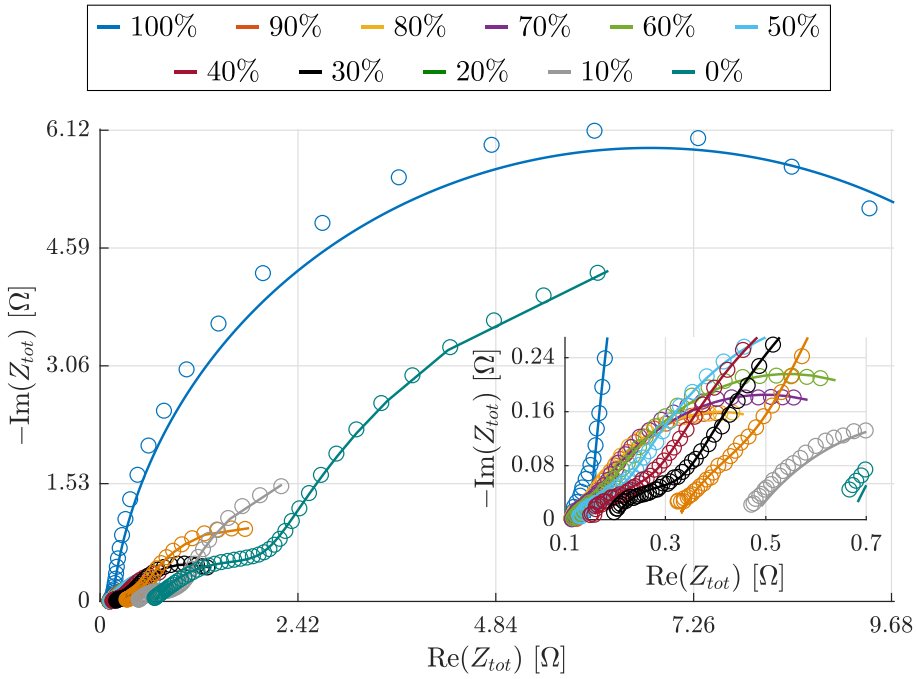

Fig. 7. GEIS at various SOC levels (100% to 0%) for Cell 7. Solid lines indicate fitted curves, while markers represent experimental data.

following first-order exponential transient model:

$$v_b = v_b(0) + (R_s + R_{\mathrm{ZnO}} + R_{ct}) \cdot \Delta i_b + R_d \cdot \Delta i_b [1 - e^{-\frac{t}{R_d \cdot C_d}}] \tag{6}$$

where Δi_b is the current step, v_b is the battery terminal voltage, and $v_b(0)$ is the battery terminal voltage at the beginning of the relaxation. Specifically, for each relaxation interval, the transient voltage profile was shifted by the initial battery terminal voltage, and the voltage drops associated with other resistance terms were subtracted so that only the transient due to diffusion was considered. Since the diffusion time constant is much larger than the other time constants (associated with the two ZARC elements), it was possible to remove the initial portion of the voltage transient related to those elements. To do this, the duration of these initial portions was set to five times the time constant of the second ZARC element, $\tau_{ct,dl}$, which represents the charge-transfer and double-layer effects and has a larger time constant than the first ZARC element. The values of $\tau_{ct,dl}$ at different SOC levels were obtained from the frequency-domain test results, as follows:

$$\tau_{ct,dl} = (R_{ct} \cdot Q_{dl})^{\frac{1}{\theta_{ct,dl}}}. \tag{7}$$

4.1.3. Frequency- and time-domain results analysis

From Figs. 8 and 9, a good agreement between the experimental data and the frequency-domain model (with the diffusion component excluded) can be observed for Cells 1–9. This is further confirmed by the coefficient of determination, R^2, which exceeds 0.99 for the real part of the impedance and 0.94 for the imaginary part across all tests. In addition, Fig. 10 shows good agreement between the experimental battery voltage transients observed during the relaxation periods and the corresponding modeled responses obtained using (7), as confirmed by an R^2 value greater than 0.91 for all tests.

All these figures are intended to illustrate the quality of the fitting procedure and to provide visual confirmation that the extracted parameters accurately capture the different dynamics during the GEIS tests and rest periods.

Fig. 11 presents the trends of the electrical parameters in (4) as a function of SOC for the different cells. From the figure, it can be observed that the parameter trends are remarkably consistent across

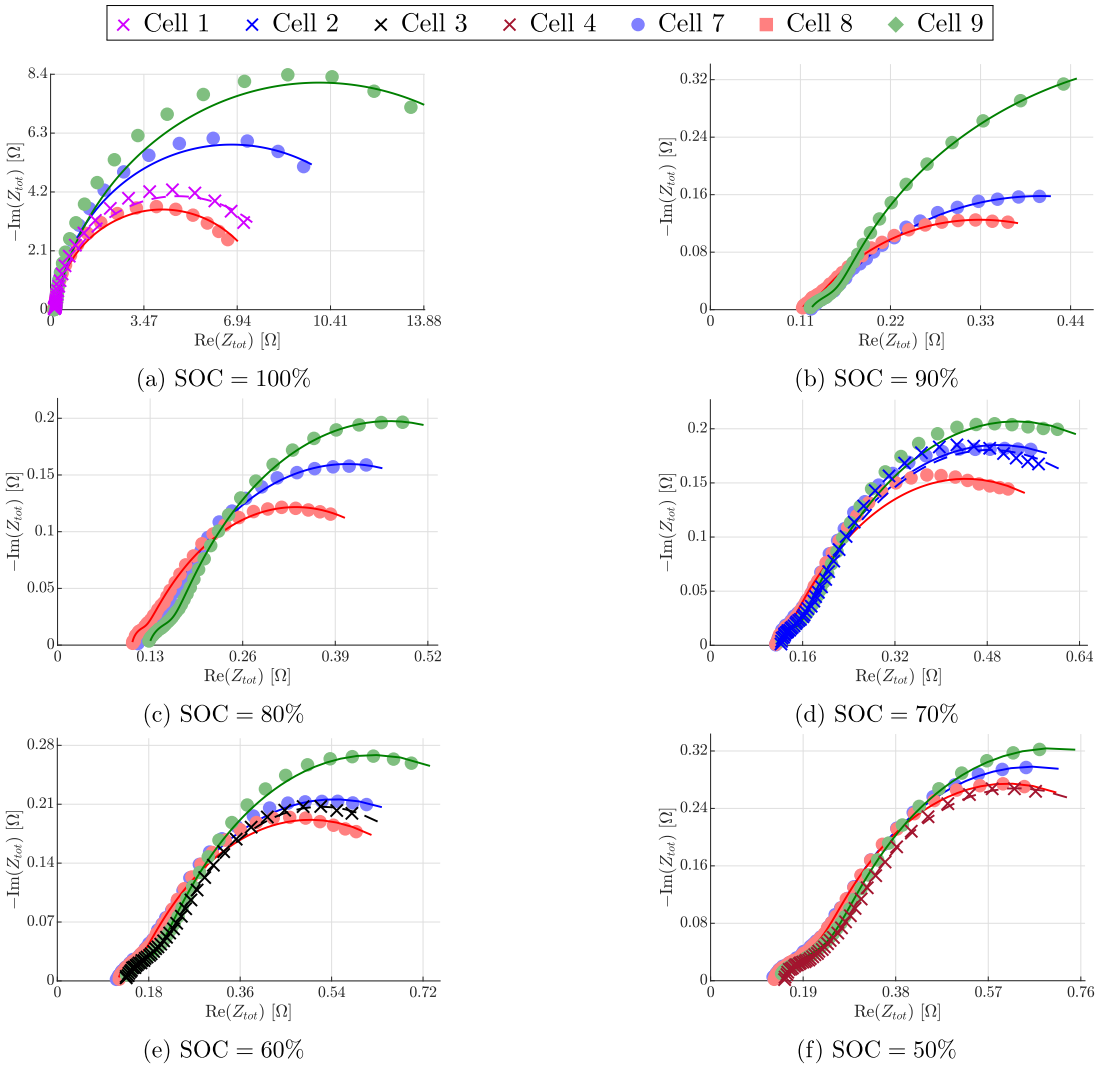

Fig. 8. GEIS at various SOC levels (100% to 50%). Solid lines indicate fitted curves, while markers represent experimental data.

Cells 1–9. This observation is further supported by the mean and standard deviation values reported in Fig. 12.

Specifically, as illustrated in Fig. 11(a), the high-frequency ohmic resistance R_s increases progressively as the cells discharge from 100% to 0% of SOC, with a pronounced rise occurring once the SOC drops below 40%.

A similar trend is observed for the resistance R_{ZnO} associated with the ZnO layer (Fig. 11(b)), which exhibits a marked increase when the SOC falls below 30%. This behavior is consistent with the progressive formation of the ZnO layer at the anode–electrolyte interface during discharge. The pseudo-capacitance Q_{ZnO}, associated with ZnO growth and shown in Fig. 11(c), is similar for all cells and does not exhibit a clear trend, remaining essentially constant throughout the discharge process. The corresponding depression factor, β_{ZnO} (Fig. 11(d)), exhibits an approximately linear decrease with decreasing SOC.

The charge-transfer resistance R_{ct}, associated with electrochemical reactions at the electrodes (Fig. 11(e)), follows a trend similar to those of R_{ZnO} and R_s in the 90%–0% of SOC range, increasing progressively during discharge and exhibiting a sharp rise once the SOC drops below 30%. On the other hand, R_{ct} also shows relatively high values at 100% of SOC, comparable to those observed at 0% of SOC. As discussed in Section 4.1, this behavior may be attributed to the instability of the electrochemical state at full charge. These results suggest that the electrochemical reactions are less favorable at 100% of SOC, become more facile after an initial discharge, and again become hindered at low SOC due to the reduction in the number of active sites on the electrodes. The related pseudo-capacitance, Q_{dl}, reported in Fig. 11(f), exhibits a sharp increase from 100% to 70% of SOC, remains relatively constant between 70% and 10% of SOC, and then decreases significantly from 10% to 0% of SOC. The corresponding depression factor, $\beta_{ct,dl}$, also reported in Fig. 11(g), shows a decreasing trend from 100% to 70% of SOC, after which it gradually increases again down to 0% of SOC. It is worth to noting that, the local minima around 30% and 70% of SOC do not appear to be mere statistical deviations, as all GEIS tests conducted on the different cells exhibit the same behavior. This phenomenon may be associated with structural phase transitions occurring within the electrodes, corresponding to the changes in slope of the OCV curve shown in Fig. 6.

Finally, the resistance component of the diffusion impedance, R_d, reported in Fig. 11(h), experiences a notable increase when the SOC falls below 10%, while the diffusion capacitance, C_d, reported in Fig. 11(i), increases as the SOC rises.

4.2. Chemical results analysis

Among the three cells (7, 8, and 9) subjected to RS, only Cell 7, deemed the most representative, is reported. The battery opening procedure enables the extraction of large portions of the cathode (see Fig. 13), allowing for a statistically meaningful analysis. The reported RS measurements are therefore representative of multiple locations

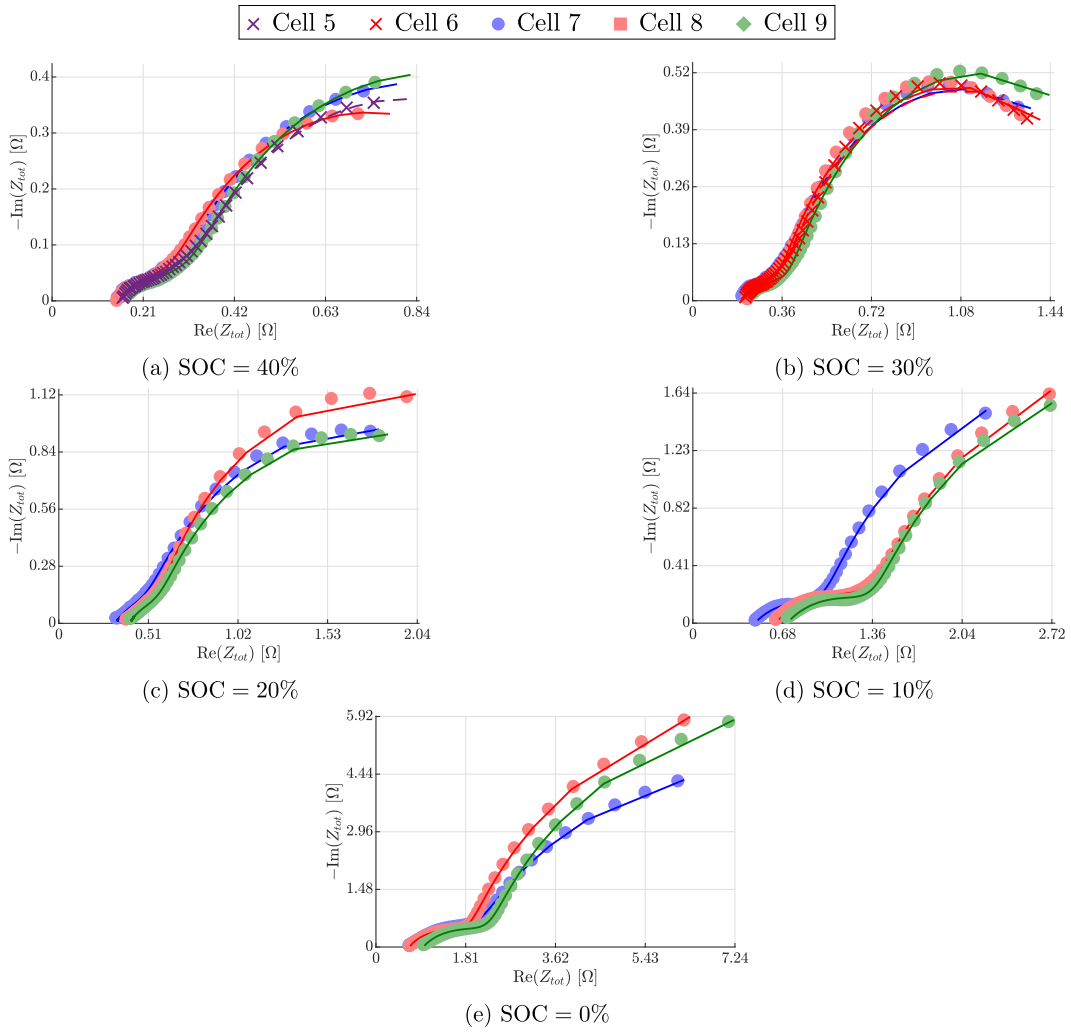

Fig. 9. GEIS at various SOC levels (40% to 0%). Solid lines indicate fitted curves, while markers represent experimental data.

examined across the cathode surface. Specifically, our investigation focused on two distinct regions: the area in direct contact with the separator (analyzed in this work) and the area adjacent to the external casing (data not shown). As expected, the latter region did not exhibit significant variations in its RS spectra, likely due to its greater distance from the separator and its consequently limited participation in the electrochemical reactions.

The anode, composed of Zn, is highly reactive upon exposure to air, which makes it unsuitable for in-depth or time-consuming post-mortem analyses. Moreover, the separator is often damaged during cell opening, exhibiting tears and localized dust formation that can interfere with RS measurements.

For these reasons, our investigation focused on the cathode surface in direct contact with the separator, where chemical modifications induced by battery cycling are most likely to occur.

The first measurements were carried out on the pristine sample. The RS spectrum (see Fig. 14) reveals two main features: the first appears between 400 cm^{-1} and 700 cm^{-1}, and the second is located around 1080 cm^{-1}. The former features are typically associated with MnO_2 structures [56], while the latter is related to carbonates. Although there is no universal consensus in the literature regarding the precise assignment of these structures [56–60]—likely due to differences in materials and cathode preparation—the RS measurements of the pristine cathode generally display the following characteristic bands: three prominent peaks at 574 cm^{-1}, 620 cm^{-1}, and 644 cm^{-1}, along with less intense bands at 290 cm^{-1}, 470 cm^{-1}, and 753 cm^{-1}. These bands correspond to various manganese oxide lattice vibrations within the octahedral manganese-oxide framework. In particular, the band at 574 cm^{-1} has been attributed to the displacement of oxygen atoms relative to manganese atoms along the octahedral chains. Moreover, variations in the intensity of the band at 644 cm^{-1} following ion exchange have been interpreted as evidence that this band is related to manganese oxide vibrations perpendicular to the direction of the octahedral double chains.

A Raman peak attributed to the symmetric stretching vibration of carbonate ions is detected in both the pristine sample and the cathode at 70% of SOC, in agreement with previous studies [61]. However, this feature disappears at deeper states of discharge. Because all SOC-extracted samples were prepared under identical environmental conditions, the most plausible explanation is electrolyte decomposition [62]. Although this behavior has been repeatedly observed, the mechanism responsible for the loss of the carbonate signal remains under active discussion within the scientific community.

When RS analysis is performed on batteries at more advanced states of discharge (specifically at 50%, 30%, and 0% of SOC), distinctive peaks corresponding to mixed zinc-manganese oxides with a spinel structure $ZnMn_2O_4$ emerge. These features, observed at 322, 383, 587, 630, and 679 cm^{-1}, are consistent with the findings reported by Nadherny [55]. Specifically, when excessive Zn^{2+} ions accumulates at the cathode, the initially layered MnO_2 structures undergo an irreversible layered-to-spinel transformation, producing spinel $ZnMn_2O_4$—a process

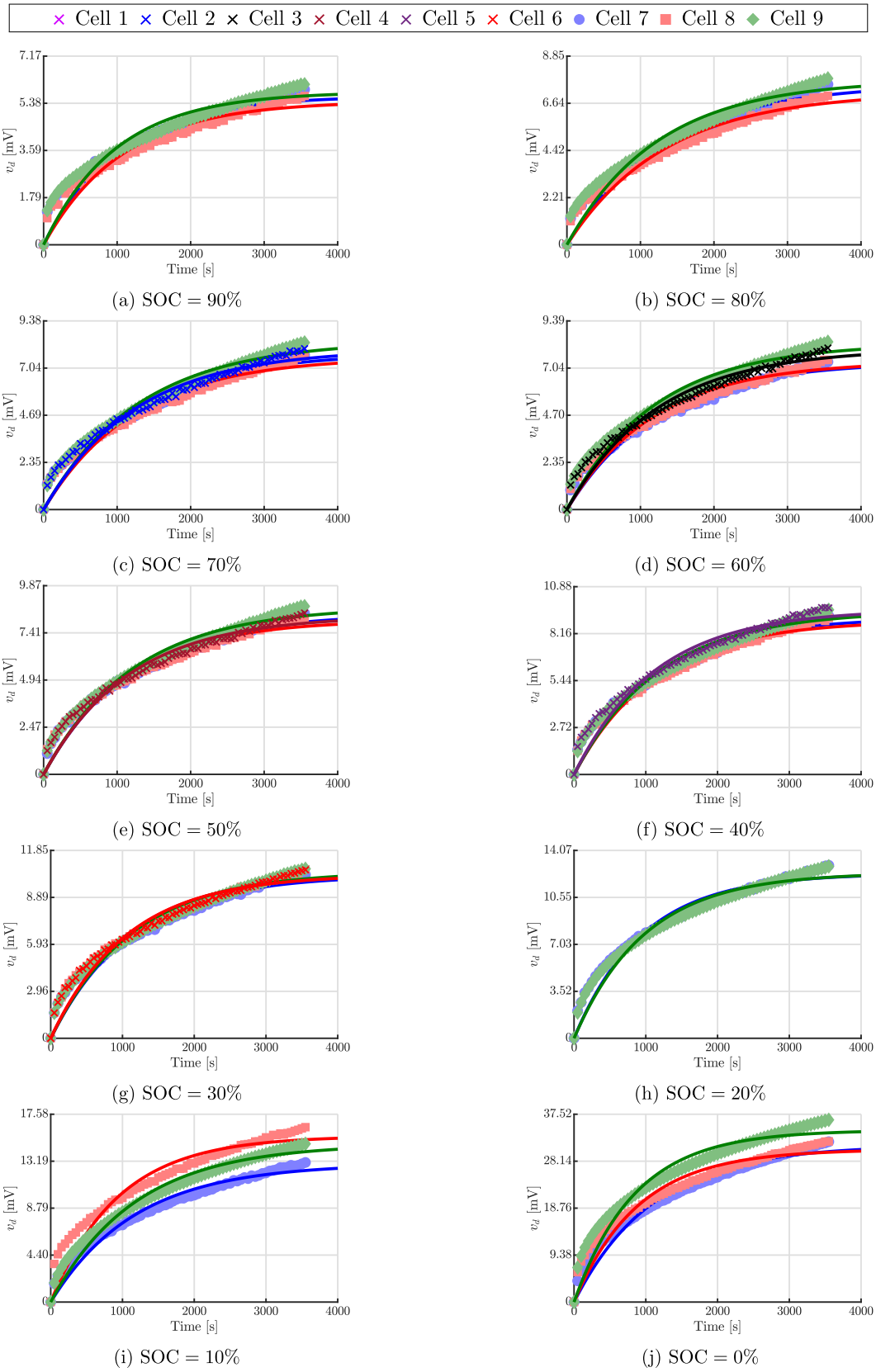

Fig. 10. Experimental data used to determine diffusion-related parameters over different SOC levels (from 90% down to 0%). Markers denote measured values, while solid lines represent the corresponding fitted curves.

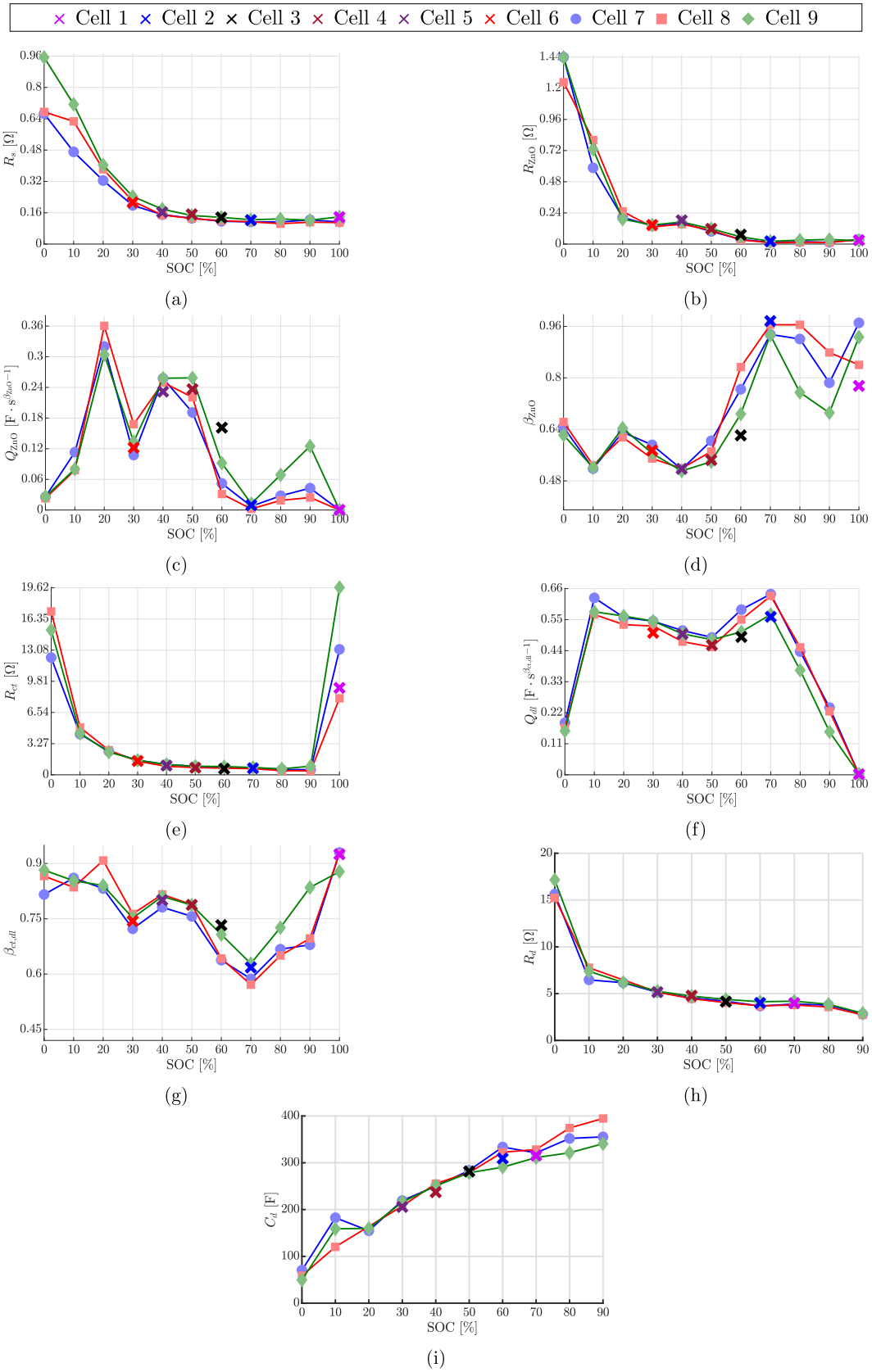

Fig. 11. Electrical parameters of the defined alkaline battery model as functions of SOC.

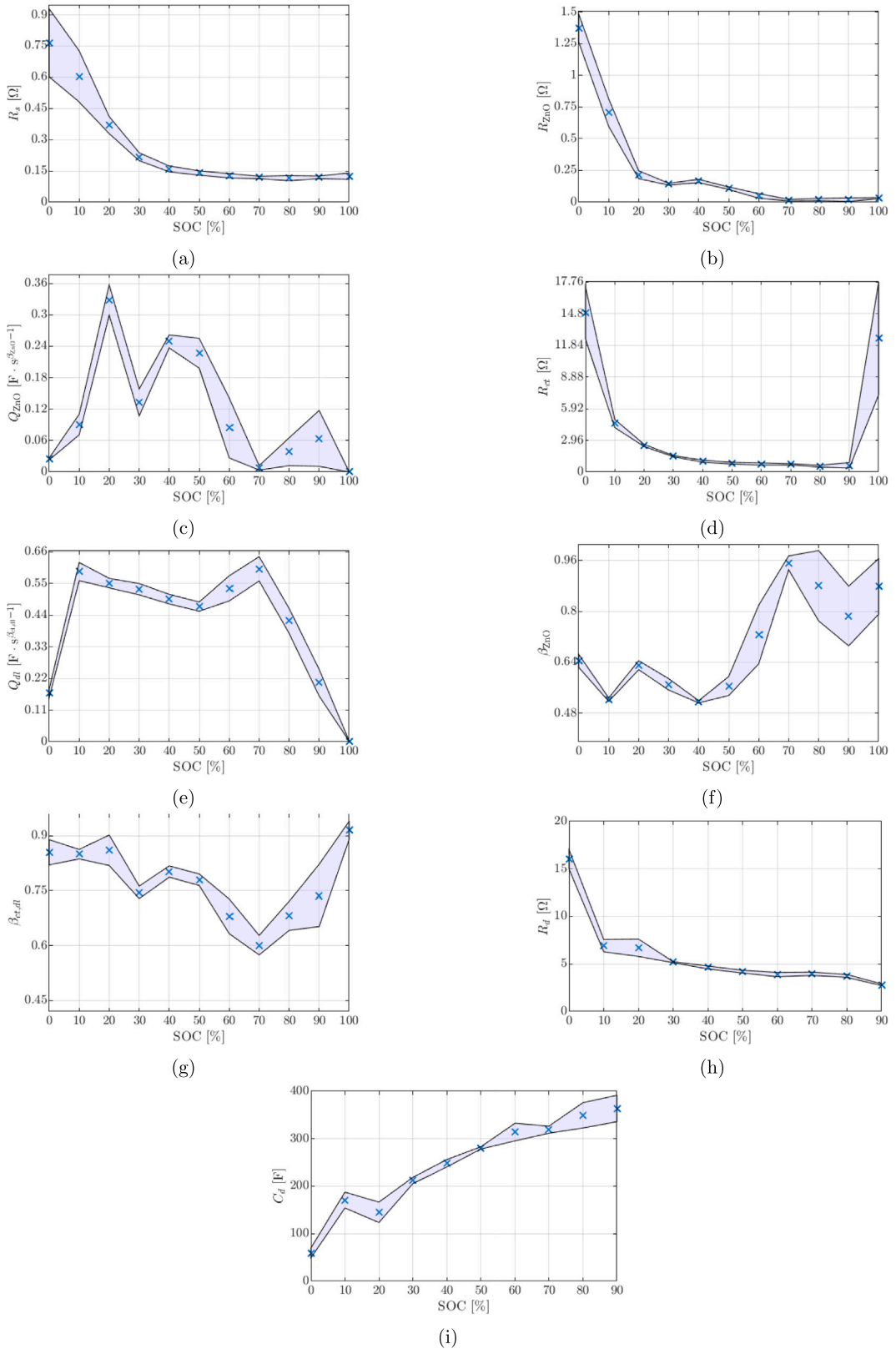

Fig. 12. Mean and standard deviation of electrical parameters of the defined alkaline battery model as functions of SOC.

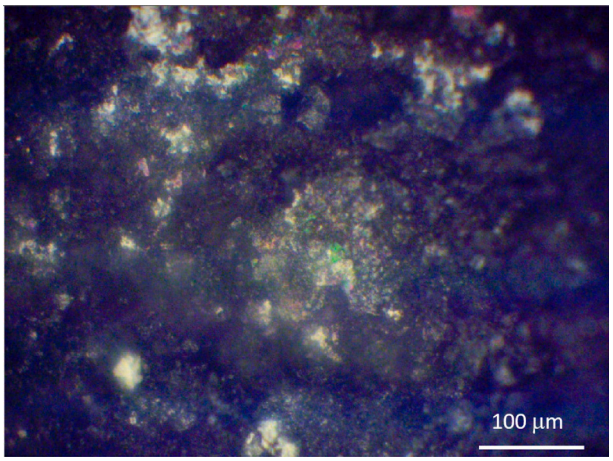

Fig. 13. Camera snapshots of the cathode area of Cell 7 investigated by RS. The employed objective is a 20x.

driven by Zn insertion and the accompanying rearrangement of manganese within the lattice [63]. We propose that the appearance and evolution of these peaks reflect cathode degradation, primarily driven by the migration of Zn-containing species through the separator. This migration process appears to be one of the key mechanisms governing the electrochemical evolution of the battery during discharge.

Overall, the regular and monotonic evolution of RS features (e.g., the $ZnMn_2O_4$ shoulder) observed during partial battery discharge underscores the critical role of this compound in influencing battery performance. We propose that the following side reaction may be involved:

$$Zn^{2+}(aq) + 2MnO_2(s) + 2e^- \rightarrow ZnMn_2O_4(s). \quad (8)$$

Controlling or mitigating this side reaction can be essential if the lifespan of alkaline batteries is to be prolonged.

4.3. Correlation between chemical and electrical results and related hypotheses

As discussed in the previous section, the high-frequency ohmic resistance R_s increases as the battery discharges from 100% to 0% of SOC. This behavior can be attributed to the progressive reduction of MnO_2, which ultimately forms Mn_2O_3, as well as to the formation of the mixed zinc-manganese spinel phase $ZnMn_2O_4$. This transformation is clearly reflected in the Raman spectra: the characteristic MnO_2 peak near 630 cm^{-1} gradually weakens and shifts slightly as the reduction proceeds, eventually disappearing at 0% of SOC. These spectral changes indicate structural and oxidation-state modifications within the cathode. In the final stage of discharge (30% to 0% of SOC), new Raman peaks appear at approximately 660 cm^{-1}, 375 cm^{-1}, and 325 cm^{-1}, which are attributed to $ZnMn_2O_4$ and intensify with further discharge, suggesting Zn incorporation into the manganese oxide lattice. These chemical transformations may be the cause of the similar trends observed for the diffusion resistance R_d across the entire SOC range, as well as for the charge-transfer resistance R_{ct} in the interval from 90% to 0% SOC.

Considering the SOC interval between 90% and 0%, and excluding the local minima around 30% and 70% of SOC, the depression factor $\beta_{ct,dl}$ (Fig. 11(g)) exhibits a consistently increasing trend. Interestingly, upon disassembling the battery, noticeable variations in the texture of the cathode material are evident at different SOC levels. At higher SOC, the cathode appears loose and fragile, whereas at lower SOC, it becomes denser and smoother. This observation suggests that $\beta_{ct,dl}$ may reflect changes in the cathode surface characteristics, corresponding to the transformation observed in RS measurements from MnO_2 to $ZnMn_2O_4$ as the discharge progresses. On the other hand, the higher value of $\beta_{ct,dl}$ at 100% of SOC, similar to the charge transfer resistance R_{ct}, may be attributed to the instability of the electrochemical state when the battery is fully charged.

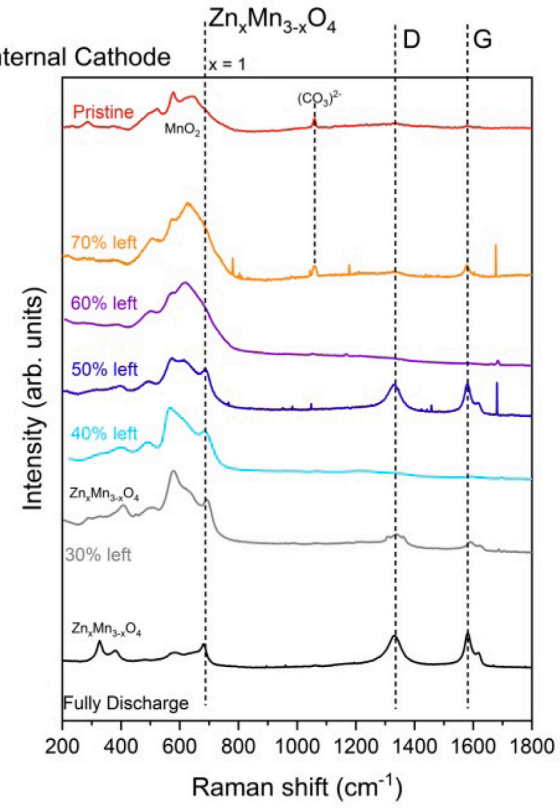

Fig. 14. RS measurements acquired on the internal cathode of Cell 7 at different SOC levels.

Although RS measurements of the anode were not performed, the increase in the resistance R_{ZnO} may be attributed to the growth of the ZnO layer, while the consistent decline in the depression factor β_{ZnO} (Fig. 11(d)) throughout discharge may indicate that the initially smooth and compact Zn surface evolves into a rougher ZnO layer. This transformation would typically be accompanied by a Raman shift from metallic Zn to ZnO in the anode region.

Additionally, as shown in Fig. 14, variations in the G and D bands of graphite can be detected. This occurrence is a direct consequence of the position of the laser beam on the cathode material that can have traces of carbonaceous materials.

5. Conclusion

This work presented a comprehensive experimental and modeling study of commercial primary alkaline batteries. Specifically, a Procell PX1604 alkaline battery was investigated by combining GEIS, time-domain relaxation analysis, and RS on the same set of cells. The main objective was to establish a physically grounded link between electrical equivalent-circuit parameters and the underlying chemical and structural evolution of the active materials during discharge.

From an electrical standpoint, a lithium-ion equivalent electrical circuit was adapted to the alkaline chemistry and systematically parametrized over the full SOC range. The proposed model comprises an high frequency ohmic resistance, a ZARC element associated with the ZnO layer at the anode, a second ZARC representing charge-transfer and double-layer effects at both electrode/electrolyte interfaces, and

a diffusion-related RC branch capturing ion-transport limitations. The identified parameters display well-defined, reproducible trends as functions of SOC across all cells, confirming both the robustness of the proposed model and the reliability of the fitting procedure.

RS provides the complementary microscopic insight required to interpret these electrical trends in terms of specific physicochemical processes. A key contribution of this work is the explicit correlation established between the Raman signatures and the evolution of the equivalent-circuit parameters extracted from frequency-domain (GEIS) and time-domain characterizations.

The progressive formation of Zn-containing spinel phases at the cathode, evidenced by the growth of the $ZnMn_2O_4$ bands, coincides with the marked increases in R_s, R_{ct}, and R_d, as well as with the changes observed in $\beta_{ct,dl}$.

On the other hand, although direct evidence is lacking since no anode chemical analysis was performed, the growth of the ZnO layer and the increase in its surface roughness may be attributed to the rise in R_{ZnO} and the reduction of the β_{ZnO} parameter observed during battery discharge.

In this perspective, the electrical model parameters acquire a clear physicochemical interpretation: ZnO layer growth and spinel formation manifest as higher ohmic and interfacial resistances and more sluggish diffusion, while changes in the depression factors encode the evolving microstructure and heterogeneity of the electrode surfaces.

The findings of this work provide a physically transparent basis for model-based simulation of alkaline batteries, enabling more realistic predictions of internal parameters and dynamic behavior as functions of SOC, and highlight concrete levers for materials and design optimization.

Even though the analyses in the present work were carried out on cylindrical cells, at room temperature, and under very low discharge rates, the methodology developed here is general and can be extended in future studies to include different discharge rates, wider temperature ranges, and various cell geometries.

CRediT authorship contribution statement

Marzio Barresi: Writing – review & editing, Writing – original draft, Validation, Methodology, Investigation, Formal analysis, Conceptualization. **Simone Barcellona:** Writing – review & editing, Writing – original draft, Validation, Methodology, Investigation, Formal analysis, Data curation, Conceptualization. **Cha Long:** Writing – original draft, Validation, Investigation, Formal analysis, Conceptualization. **Lorenzo Codecasa:** Writing – review & editing, Supervision. **Marco Menegazzo:** Writing – review & editing. **Rossella Yivlialin:** Writing – review & editing. **Eugenio Gibertini:** Writing – review & editing. **Andrea Lucotti:** Writing – review & editing, Formal analysis. **Gianlorenzo Bussetti:** Writing – review & editing, Writing – original draft, Supervision, Resources, Investigation, Formal analysis. **Samuele Grillo:** Writing – review & editing, Supervision, Resources.

Declaration of competing interest

The authors declare that they have no known competing financial interests or personal relationships that could have appeared to influence the work reported in this paper.

Acknowledgments

The authors would like to thank ACCU ITALIA S.p.A. for the provision of the battery cells used in the experiments.

The Raman spectroscopy experiments have been performed at the Solid-Liquid Interface Nanomicroscopy and Spectroscopy laboratory which is an interdepartmental facility at Politecnico di Milano.

M. Barresi and S. Grillo partially funded by the EU fund Next Generation EU, Missione 4, Componente 2, Investimento 1.3 CUP D43C22003090001, PE0000021 PNRR NEST Spoke 6.

Data availability

The data are deposited in a GitHub repository associated with this work.

References

[1] N.G. Chatzigeorgiou, S. Theocharides, G. Makrides, G.E. Georghiou, A review on battery energy storage systems: Applications, developments, and research trends of hybrid installations in the end-user sector, J. Energy Storage 86 (2024) 111192, http://dx.doi.org/10.1016/j.est.2024.111192, URL https://www.sciencedirect.com/science/article/pii/S2352152X2400776X.

[2] Y. Yang, R. Wang, Z. Shen, Q. Yu, R. Xiong, W. Shen, Towards a safer lithium-ion batteries: A critical review on cause, characteristics, warning and disposal strategy for thermal runaway, Adv. Appl. Energy 11 (2023) 100146, http://dx.doi.org/10.1016/j.adapen.2023.100146, URL https://www.sciencedirect.com/science/article/pii/S2666792423000252.

[3] P. Phogat, S. Dey, M. Wan, Powering the sustainable future: a review of emerging battery technologies and their environmental impact, RSC Sustain. 3 (2025) 3266–3306, http://dx.doi.org/10.1039/D5SU00127G.

[4] J. Thakur, P. Phogat, Shreya, R. Jha, S. Singh, Non-rechargeable batteries: a review of primary battery technology and future trends, Phys. Chem. Chem. Phys. 27 (2025) 4045–4077, http://dx.doi.org/10.1039/D4CP04614E.

[5] E.S. Takeuchi, K.J. Takeuchi, A.C. Marschilok, The ongoing importance of lithium primary batteries: 50+ years and going strong, ECS Meet. Abstr. MA2022-02 (2) (2022) 102, http://dx.doi.org/10.1149/MA2022-022102mtgabs.

[6] Section 2 - rechargeable cells and batteries, in: Rechargeable Batteries Applications Handbook, in: EDN Series for Design Engineers, Newnes, Newton, 1998, pp. 5–33, http://dx.doi.org/10.1016/B978-075067006-7/50003-6, URL https://www.sciencedirect.com/science/article/pii/B9780750670067500036.

[7] S. Hemavathi, S. Srirama, A.S. Prakash, Present and future generation of secondary batteries: A review, ChemBioEng Rev. 10 (6) (2023) 1123–1145, http://dx.doi.org/10.1002/cben.202200040, URL https://onlinelibrary.wiley.com/doi/abs/10.1002/cben.202200040.

[8] R. Xiong, Q. Yu, L.Y. Wang, C. Lin, A novel method to obtain the open circuit voltage for the state of charge of lithium ion batteries in electric vehicles by using H infinity filter, Appl. Energy 207 (2017) 346–353, http://dx.doi.org/10.1016/j.apenergy.2017.05.136, Transformative Innovations for a Sustainable Future – Part II, URL https://www.sciencedirect.com/science/article/pii/S0306261917306852.

[9] M. Elmahallawy, T. Elfouly, A. Alouani, A.M. Massoud, A comprehensive review of lithium-ion batteries modeling, and state of health and remaining useful lifetime prediction, IEEE Access 10 (2022) 119040–119070, http://dx.doi.org/10.1109/ACCESS.2022.3221137.

[10] W.J. Wruck, Phd thesis, The University of Wisconsin, Madison, WI, 1984.

[11] J.S. Newman, Electrochemical Systems, A JOHN WILEY & SONS, INC PUBLICATION, 1991.

[12] J.-S. Chen, H.Y. Cheh, Modeling of cylindrical alkaline cells: III . Mixed-reaction model for the anode, J. Electrochem. Soc. 140 (5) (1993) 1205, http://dx.doi.org/10.1149/1.2220958.

[13] J.-S. Chen, H.Y. Cheh, Modeling of cylindrical alkaline cells: IV . Dissolution-precipitation model for the anode, J. Electrochem. Soc. 140 (5) (1993) 1213, http://dx.doi.org/10.1149/1.2220959.

[14] E.J. Podlaha, H.Y. Cheh, Modeling of cylindrical alkaline cells: V . High discharge rates, J. Electrochem. Soc. 141 (1) (1994) 15, http://dx.doi.org/10.1149/1.2054677.

[15] E.J. Podlaha, H.Y. Cheh, Modeling of cylindrical alkaline cells: VI . Variable discharge conditions, J. Electrochem. Soc. 141 (1) (1994) 28, http://dx.doi.org/10.1149/1.2054701.

[16] Y. Zhang, H.Y. Cheh, Modeling of cylindrical alkaline cells VIII. Solution of the model by exploiting its differential algebraic equation structure, J. Electrochem. Soc. 146 (3) (1999) 850, http://dx.doi.org/10.1149/1.1391691.

[17] Y. Zhang, H.Y. Cheh, Modeling of cylindrical alkaline cells: IX. A rigorous mathematical model for sensitivity analysis, J. Electrochem. Soc. 146 (10) (1999) 3566, http://dx.doi.org/10.1149/1.1392515.

[18] T.W. Farrell, C.P. Please, D.L.S. McElwain, D.A.J. Swinkels, Primary alkaline battery cathodes a three-scale model, J. Electrochem. Soc. 147 (11) (2000) 4034, http://dx.doi.org/10.1149/1.1394015.

[19] S.W. Donne, J.H. Kennedy, Electrochemical impedance spectroscopy of the alkaline manganese dioxide electrode, J. Appl. Electrochem. 34 (2004) 159–168, http://dx.doi.org/10.1023/B:JACH.0000009946.01158.ca.

[20] J.B. Arnott, G.J. Browning, S.W. Donne, Study on manganese dioxide discharge using electrochemical impedance spectroscopy, J. Electrochem. Soc. 153 (7) (2006) A1332, http://dx.doi.org/10.1149/1.2198147.

[21] M.R. Bailey, S.W. Donne, Electrochemical impedance spectroscopy study into the effect of titanium dioxide added to the alkaline manganese dioxide cathode, J. Electrochem. Soc. 158 (7) (2011) A802, http://dx.doi.org/10.1149/1.3586045.

[22] E. Ferg, F. van Vuuren, Comparative capacity performance and electrochemical impedance spectroscopy of commercial AA alkaline primary cells, Electrochim. Acta 128 (2014) 203–209, http://dx.doi.org/10.1016/j.electacta.2013.08.110, Advances in Electrochemical Materialsscience and Manufacturing, URL https://www.sciencedirect.com/science/article/pii/S001346861301640X.

[23] L. Hu, X. Xu, Current pulse-based measurement technique for zinc–air battery parameters, Energies 16 (18) (2023) http://dx.doi.org/10.3390/en16186448, URL https://www.mdpi.com/1996-1073/16/18/6448.

[24] R. Franke-Lang, J. Kowal, Analysis of electrochemical impedance spectroscopy on zinc-air batteries using the distribution of relaxation times, Batteries 7 (3) (2021) http://dx.doi.org/10.3390/batteries7030056, URL https://www.mdpi.com/2313-0105/7/3/56.

[25] J. Macdonald, W. Johnson, I. Raistrick, D. Franceschetti, N. Wagner, M. McKubre, D. Macdonald, B. Sayers, N. Bonanos, B. Steele, E. Butler, W. Worell, G. Niklasson, S. Malmgren, M. Stromme, S. Sundaram, G. Engelhardt, E. Barsoukov, B. Conway, W. Pell, C. Roland, R. Eisenberg, in: E. Barsoukov, J. Macdonald (Eds.), Impedance Spectroscopy: Theory, Experiment, and Applications, third ed., John Wiley & Sons, 2018, pp. 424–458, 3 überarbeitete Ausgabe, Monographie mit über 528 Seiten, URL https://elib.dlr.de/121440/.

[26] M. Gaberšček, Impedance spectroscopy of battery cells: Theory versus experiment, Curr. Opin. Electrochem. 32 (2022) 100917, http://dx.doi.org/10.1016/j.coelec.2021.100917, URL https://www.sciencedirect.com/science/article/pii/S2451910321002313.

[27] C. Woosung, S. Heon-Cheol, K.J. Man, C. Jae-Young, Y. Won-Sub, Modeling and applications of electrochemical impedance spectroscopy (EIS) for lithium-ion batteries, J. Electrochem. Sci. Technol 11 (1) (2020) 1–13, http://dx.doi.org/10.33961/jecst.2019.00528, URL http://jecst.org/journal/view.php?number=315.

[28] N.S. Kaisare, V. Ramani, K. Pushpavanam, S. Ramanathan, An analysis of drifts and nonlinearities in electrochemical impedance spectra, Electrochim. Acta 56 (22) (2011) 7467–7475, http://dx.doi.org/10.1016/j.electacta.2011.06.112, URL https://www.sciencedirect.com/science/article/pii/S0013468611010097.

[29] M. Flannagin, B. Barnes, W. O'Donoghue, J. Mayeur, K. Hazeli, G.J. Nelson, Electrochemical response of alkaline batteries subject to quasi-static and dynamic loading, J. Electrochem. Soc. 170 (1) (2023) 010521, http://dx.doi.org/10.1149/1945-7111/acaad0.

[30] W. Vermeer, G.R. Chandra Mouli, P. Bauer, A comprehensive review on the characteristics and modeling of lithium-ion battery aging, IEEE Trans. Transp. Electrification 8 (2) (2022) 2205–2232, http://dx.doi.org/10.1109/TTE.2021.3138357.

[31] F. Rossi, E. Marini, M. Boniardi, A. Casaroli, A.L. Bassi, A. Macrelli, C. Mele, B. Bozzini, What happens to MnO2 when it comes in contact with Zn2+? An electrochemical study in aid of Zn/MnO2-based rechargeable batteries, Energy Technol. 10 (8) (2022) 2200084, http://dx.doi.org/10.1002/ente.202200084, URL https://onlinelibrary.wiley.com/doi/abs/10.1002/ente.202200084.

[32] W.-B. Cai, Q. Shi, M.F. Mansuetto, D.A. Scherson, In situ Raman spectroscopy on an operating AA Zn-MnO2 battery under high discharge currents, Electrochem. Solid-State Lett. 3 (7) (2000) 319, http://dx.doi.org/10.1149/1.1391135.

[33] J. Zuo, C. Xu, Y. Liu, Y. Qian, Crystallite size effects on the Raman spectra of Mn3O4, Nanostruct. Mater. 10 (8) (1998) 1331–1335, http://dx.doi.org/10.1016/S0965-9773(99)00002-1, URL https://www.sciencedirect.com/science/article/pii/S0965977399000021.

[34] S. Bernardini, F. Bellatreccia, A. Casanova Municchia, G. Della Ventura, A. Sodo, Raman spectra of natural manganese oxides, J. Raman Spectrosc. 50 (6) (2019) 873–888, http://dx.doi.org/10.1002/jrs.5583, URL https://analyticalsciencejournals.onlinelibrary.wiley.com/doi/abs/10.1002/jrs.5583.

[35] J.E. Post, D.A. McKeown, P.J. Heaney, Raman spectroscopy study of manganese oxides: Layer structures, Am. Mineral. 106 (3) (2021) 351–366, http://dx.doi.org/10.2138/am-2021-7666.

[36] B. Zhang, P. Dong, S. Yuan, Y. Zhang, Y. Zhang, Y. Wang, Manganese-based oxide cathode materials for aqueous zinc-ion batteries: Materials, mechanism, challenges, and strategies, Chem & Bio Eng. 1 (2) (2024) 113–132, http://dx.doi.org/10.1021/cbe.3c00120.

[37] F. Chen, Y. Zhang, S. Chen, H. Zang, C. Liu, H. Sun, B. Geng, Regulating the kinetics of zinc-ion migration in spinel ZnMn2O4 through iron doping boosted aqueous zinc-ion storage performance, J. Colloid Interface Sci. 649 (2023) 703–712, http://dx.doi.org/10.1016/j.jcis.2023.06.152, URL https://www.sciencedirect.com/science/article/pii/S0021979723011797.

[38] D. Linden, T.B. Reddy, in: E. Barsoukov, J. Macdonald (Eds.), Handbook of Batteries, McGraw-Hill Companies, 2002.

[39] N.C. Cahoon, M.P. Korver, The cathodic reduction of manganese dioxide in alkaline electrolyte, J. Electrochem. Soc. 106 (9) (1959) 745, http://dx.doi.org/10.1149/1.2427490.

[40] Y. Chabre, J. Pannetier, Structural and electrochemical properties of the proton / γ-MnO2 system, Prog. Solid State Chem. 23 (1) (1995) 1–130, http://dx.doi.org/10.1016/0079-6786(94)00005-2, URL https://www.sciencedirect.com/science/article/pii/0079678694000052.

[41] S. Barcellona, L. Piegari, Lithium ion battery models and parameter identification techniques, Energies 10 (12) (2017) 2007, http://dx.doi.org/10.3390/en10122007, URL http://www.mdpi.com/1996-1073/10/12/2007.

[42] H. He, R. Xiong, J. Fan, Evaluation of lithium-ion battery equivalent circuit models for state of charge estimation by an experimental approach, Energies 4 (4) (2011) 582–598, http://dx.doi.org/10.3390/en4040582, URL https://www.mdpi.com/1996-1073/4/4/582.

[43] Y.-H. Kim, H.-D. Ha, Design of interface circuits with electrical battery models, IEEE Trans. Ind. Electron. 44 (1) (1997) 81–86, http://dx.doi.org/10.1109/41.557502.

[44] F. Feng, R. Lu, G. Wei, C. Zhu, Online estimation of model parameters and state of charge of LiFePO4 batteries using a novel open-circuit voltage at various ambient temperatures, Energies 8 (4) (2015) 2950–2976, http://dx.doi.org/10.3390/en8042950, URL https://www.mdpi.com/1996-1073/8/4/2950.

[45] C. Zhang, W. Allafi, Q. Dinh, P. Ascencio, J. Marco, Online estimation of battery equivalent circuit model parameters and state of charge using decoupled least squares technique, Energy 142 (2018) 678–688, http://dx.doi.org/10.1016/j.energy.2017.10.043, URL https://www.sciencedirect.com/science/article/pii/S0360544217317127.

[46] A. Hentunen, T. Lehmuspelto, J. Suomela, Time-domain parameter extraction method for Thévenin-equivalent circuit battery models, IEEE Trans. Energy Convers. 29 (3) (2014) 558–566, http://dx.doi.org/10.1109/TEC.2014.2318205.

[47] D. Andre, M. Meiler, K. Steiner, C. Wimmer, T. Soczka-Guth, D. Sauer, Characterization of high-power lithium-ion batteries by electrochemical impedance spectroscopy. I. Experimental investigation, J. Power Sources 196 (12) (2011) 5334–5341, http://dx.doi.org/10.1016/j.jpowsour.2010.12.102, Selected papers presented at the 12th Ulm ElectroChemical Talks (UECT):2015 Technologies on Batteries and Fuel Cells, URL https://www.sciencedirect.com/science/article/pii/S0378775311000681.

[48] X. Wang, X. Wei, H. Dai, Estimation of state of health of lithium-ion batteries based on charge transfer resistance considering different temperature and state of charge, J. Energy Storage 21 (2019) 618–631, http://dx.doi.org/10.1016/j.est.2018.11.020, URL https://www.sciencedirect.com/science/article/pii/S2352152X18305279.

[49] J. Estaller, A. Kersten, M. Kuder, T. Thiringer, R. Eckerle, T. Weyh, Overview of battery impedance modeling including detailed state-of-the-art cylindrical 18650 lithium-ion battery cell comparisons, Energies 15 (10) (2022) http://dx.doi.org/10.3390/en15103822, URL https://www.mdpi.com/1996-1073/15/10/3822.

[50] M.E. Orazem, B. Ulgut, On the use of drift correction for electrochemical impedance spectroscopy measurements, Electrochim. Acta 443 (2023) 141959, http://dx.doi.org/10.1016/j.electacta.2023.141959, URL https://www.sciencedirect.com/science/article/pii/S0013468623001469.

[51] M.A. Zabara, G. Katırcı, B. Ülgüt, Non-linear harmonics in EIS of batteries with lithium anodes: Proper controls and analysis, Electrochim. Acta 429 (2022) 140969, http://dx.doi.org/10.1016/j.electacta.2022.140969, URL https://www.sciencedirect.com/science/article/pii/S0013468622011264.

[52] B.A. Boukamp, Impedance Spectroscopy, Strength and Limitations (Impedanzspektroskopie, Stärken und Grenzen), Tm - Tech. Mess. 71 (9) (2004) 454–459, http://dx.doi.org/10.1524/teme.71.9.454.42758.

[53] M. Messing, T. Shoa, S. Habibi, Electrochemical impedance spectroscopy with practical rest-times for battery management applications, IEEE Access 9 (2021) 66989–66998, http://dx.doi.org/10.1109/ACCESS.2021.3077211.

[54] Y. Fernández Pulido, C. Blanco, D. Anseán, V.M. García, F. Ferrero, M. Valledor, Determination of suitable parameters for battery analysis by electrochemical impedance spectroscopy, Measurement 106 (2017) 1–11, http://dx.doi.org/10.1016/j.measurement.2017.04.022, URL https://www.sciencedirect.com/science/article/pii/S0263224117302476.

[55] L. Nádherný, M. Maryško, D. Sedmidubský, C. Martin, Structural and magnetic properties of ZnxMn3-xO4 spinels, J. Magn. Magn. Mater. 413 (2016) 89–96, http://dx.doi.org/10.1016/j.jmmm.2016.04.029, URL https://www.sciencedirect.com/science/article/pii/S0304885316303432.

[56] U. Siamionau, Y. Aniskevich, A. Mazanik, O. Kokits, G. Ragoisha, J.H. Jo, S.-T. Myung, E. Streltsov, Rechargeable zinc-ion batteries with manganese dioxide cathode: How critical is choice of manganese dioxide polymorphs in aqueous solutions? J. Power Sources 523 (2022) 231023, http://dx.doi.org/10.1016/j.jpowsour.2022.231023, URL https://www.sciencedirect.com/science/article/pii/S0378775322000477.

[57] R. Leardi, Experimental design in chemistry: A tutorial, Anal. Chim. Acta 652 (1) (2009) 161–172, http://dx.doi.org/10.1016/j.aca.2009.06.015, Fundamental and Applied Analytical Science. A Special Issue In Honour of Alan Townshend, URL https://www.sciencedirect.com/science/article/pii/S0003267009008058.

[58] C.S. Goh, J. Wei, L.C. Lee, M. Gupta, Development of novel carbon nanotube reinforced magnesium nanocomposites using the powder metallurgy technique, Nanotechnology 17 (1) (2005) 7, http://dx.doi.org/10.1088/0957-4484/17/1/002.

[59] C. Julien, M. Massot, C. Poinsignon, Lattice vibrations of manganese oxides: Part I. Periodic structures, Spectrochim. Acta Part A: Mol. Biomol. Spectrosc. 60 (3) (2004) 689–700, http://dx.doi.org/10.1016/S1386-1425(03)00279-8, URL https://www.sciencedirect.com/science/article/pii/S1386142503002798.

[60] C. Julien, M. Massot, Raman scattering of LiNi1-yAlyO2, Solid State Ion. 148 (1) (2002) 53–59, http://dx.doi.org/10.1016/S0167-2738(02)00117-0, URL https://www.sciencedirect.com/science/article/pii/S0167273802001170.

[61] T. Wang, M. Kunimoto, T. Mori, M. Yanagisawa, J. Niikura, I. Takahashi, M. Morita, T. Abe, T. Homma, Carbonate formation on carbon electrode in rechargeable zinc-air battery revealed by in-situ Raman measurements, J. Power Sources 533 (2022) 231237, http://dx.doi.org/10.1016/j.jpowsour.2022.231237, URL https://www.sciencedirect.com/science/article/pii/S0378775322002555.

[62] T. Wang, M. Kunimoto, T. Mori, M. Yanagisawa, J. Niikura, I. Takahashi, M. Morita, T. Abe, T. Homma, Carbonate formation on carbon electrode in rechargeable zinc-air battery revealed by in-situ Raman measurements, J. Power Sources 533 (2022) 231237, http://dx.doi.org/10.1016/j.jpowsour.2022.231237, URL https://www.sciencedirect.com/science/article/pii/S0378775322002555.

[63] X. Wu, Y. Xiang, Q. Peng, X. Wu, Y. Li, F. Tang, R. Song, Z. Liu, Z. He, X. Wu, Green-low-cost rechargeable aqueous zinc-ion batteries using hollow porous spinel ZnMn2O4 as the cathode material, J. Mater. Chem. A 5 (2017) 17990–17997, http://dx.doi.org/10.1039/C7TA00100B.